Original article

Infrasonic Oscillations in Ionosphere and Their Manifestations in Hydrosphere

G. I. Dolgikh [1], M. A. Bolsunovskii [1, 2], S. G. Dolgikh [1, 2, ✉]

[1] *V.I. Il'ichev Pacific Oceanological Institute, Far Eastern Branch of Russian Academy of Sciences, Vladivostok, Russian Federation*
[2] *Institute of Automation and Control Processes, Far Eastern Branch of Russian Academy of Sciences, Vladivostok, Russian Federation*
✉ *sdolgikh@poi.dvo.ru*

Abstract
Purpose. The aim of this study is to identify and analyze the main infrasonic oscillatory processes observed in records from sea level measuring stations and stations of global navigation satellite systems (GNSS), as well as to determine the primary sources of these oscillations.
Methods and Results. Ionospheric GNSS data from stations located in the Primorsky Territory of Russia and sea level data from marine stations in the Pacific Ocean and the Sea of Japan were analyzed. Variations in total electron content (TEC) and sea level were examined, and the dominant oscillation periods in the ionosphere and hydrosphere corresponding to specific measurement sites were compared. Spectral analysis was performed using two different methods: the periodogram method and the maximum likelihood estimation (MLE) method. The results show that the dominant oscillation periods in the ionosphere above water areas coincide with those of sea surface fluctuations, with an average deviation of 2.5%. Two independent experiments indicate that these oscillations originate in the atmosphere and subsequently excite oscillations of similar periods in the hydrosphere.
Conclusions. Analysis of ionospheric TEC variations and data from level measuring stations demonstrates that the periods of the dominant spectral maxima are in good agreement with high accuracy. The obtained results indicate that the oscillation periods the ionosphere and the hydrosphere correspond to the same eigen atmospheric oscillations over specific territories and water areas. The observed coincidence of oscillation periods confirms strong coupling between atmospheric infrasonic disturbances, the ionosphere, and the hydrosphere. In the future, integrated experiments with modern laser interferometric systems will allow for a better understanding of the mechanisms of interaction between geospheres.

Keywords: infrasonic oscillations, ionosphere, hydrosphere, GNSS, total electron content, atmosphere-ocean coupling, spectral analysis

Acknowledgments: The authors thank the staff of the Laboratory of Physics of Geospheres for their assistance and support. This work was supported by project No. 124022100074-9 "Study of the nature of linear and nonlinear interaction of geospheric fields of the transitional zones of the World Ocean and their consequences", and by the Russian Science Foundation grant No. 22-17-00121 "Emergence, development and transformation of geospheric processes of the infrasound range".

For citation: Dolgikh, G.I., Bolsunovskii, M.A. and Dolgikh, S.G., 2026. Infrasonic Oscillations in the Ionosphere and Their Manifestations in the Hydrosphere. *Physical Oceanography*, 33(1), pp. 107-126.

© 2026, G. I. Dolgikh, M. A. Bolsunovskii, S. G. Dolgikh

© 2026, Physical Oceanography

Introduction

The study of interactions between geospheres is one of the fundamental problems of modern science. Understanding the mechanisms governing interactions within the lithosphere–hydrosphere–atmosphere system is particularly important in

The content is available under Creative Commons Attribution-NonCommercial 4.0 International (CC BY-NC 4.0) License

the context of the rapid development and globalization of technological systems, which require timely diagnosis and forecasting of environmental conditions.

For example, the movement and interaction of lithospheric plates and blocks lead to seismic activity, which serves as a source of numerous effects not only within the lithosphere itself but also in various layers of the atmosphere and hydrosphere. An earthquake represents a complex source of acoustic and electromagnetic impacts on the Earth's atmosphere and ionosphere.

According to current understanding, one of the primary mechanisms of energy and momentum transfer from the Earth's surface to the upper layers of the atmosphere is the propagation of internal atmospheric waves. Under favorable conditions, such waves can reach ionosphere altitudes (90–400 km) and induce perturbations in the ionospheric plasma through interactions between neutral and charged components. These internal atmospheric waves most commonly manifest in the ionosphere as travelling ionospheric disturbances. The sources of such ionospheric perturbations may include both the main seismic shock and seismic Rayleigh surface waves propagating over long distances.

Ionospheric perturbations have been detected following more than 50 major earthquakes. Significant progress in this field has been achieved over the past two decades owing to the development of ionosphere sensing methods based on signals from GNSS, such as GPS and GLONASS [1–4].

Using measurements of GNSS radio signals, the total electron content (TEC) in the ionosphere is determined along the line of sight between a GNSS satellite and a ground-based receiver. The TEC reflects the behavior of electron density and its variations caused by various physical processes. The high accuracy of TEC determination from phase measurements at two GNSS operating frequencies enables the investigation of a wide range of ionospheric perturbations.

Ionospheric monitoring using networks of ground-based GNSS receivers makes it possible to detect travelling ionospheric disturbances generated by earthquakes, tsunamis [5], volcanic eruptions and explosions [6], nuclear tests [7], microbaroms produced by standing ocean waves, and other processes occurring in adjacent geospheres.

In the context of global climate change and the ongoing increase in mean global temperature, it is necessary to consider not only greenhouse gas emissions but also the contribution of energy dissipation processes within the geospheres, which are largely associated with the increasing frequency and intensity of catastrophic natural phenomena.

The amplitude and form of ionospheric perturbations recorded by GNSS depend on several factors, including earthquake parameters, the background state of the ionosphere, GNSS satellites observation geometry, and the orientation of the geomagnetic field. In addition to these known sources of ionospheric disturbances across various frequency ranges, particular attention should be paid to perturbations associated with the intrinsic properties of the ionospheric layers themselves, namely their natural oscillation modes (eigenoscillations).

Of particular interest are the background state of the ionosphere and the spectral range of ionospheric oscillations excited by external impulsive forcing. One such perturbation source is the eruption of the Hunga Tonga–Hunga Ha'apai volcano [8], as well as other impulsive disturbances originating in adjacent geospheres, such as

earthquakes. However, other contributing factors may also play a role, including differences in the vertical motion of ocean and land surfaces [1], background atmospheric winds, and possible extraterrestrial sources.

When studying ionospheric eigenoscillations, attention should be focused on identifying the presence of characteristic oscillation periods at different time intervals under various external stimuli. An additional approach to determining the eigenoscillation periods involves examining their manifestation in independent physical processes.

The first step in addressing this problem – namely, determining the periods of ionospheric eigenoscillations in the range of 6–40 min – requires selecting an appropriate object of study. In this work, the object of study is GNSS-derived TEC data of the ionosphere measured along the line of sight between GNSS satellites and ground-based receivers. The analysis is focused on a specific region, namely the southern part of the Primorsky Territory of Russia and the Japanese Islands.

The main objective of this study is to research the mechanisms of atmospheric processes affecting the hydrosphere, as well as to determine the primary source of recorded geospheric disturbances. The main research method was comparison of maxima of the oscillation periods of the two geospheres, using the MLE method and the periodogram method. The applied approach allows us to determine the mechanism of interaction and the primary source of the detected fluctuations.

Materials and methods

In this study, GNSS data are used to analyze variations in the TEC of the ionosphere measured along the line of sight between GNSS satellites and ground-based receivers. The data were obtained from the GLONASS satellite systems (24 satellites operating at altitudes of 18,840–19,440 km) and GPS (32 satellites operating at an altitude of approximately 20,150 km). TEC measurements were collected from a network of ground-based GNSS stations located in the Primorsky Territory of Russia, including ARSN, BKM2, DLNG, IMAN, KALV, LESO, NKHD, NOVP, SHUL, SLAV, VLAD, VLDV, and ZAPV (Fig. 1).

The ground projections of the orbits of the GNSS satellites considered in this study pass over multiple land and marine areas. GNSS receiving stations located in the Primorsky Territory record variations in the TEC of the ionosphere along the line of sight between a satellite and a ground-based receiver. Thus, the primary experimental data used in this study are time series of TEC variations.

TEC is an integral measure of electron density, characterizing the total number of free electrons along the signal path through the entire thickness of the ionosphere. The main contribution to TEC is provided by ionospheric layers located at altitudes of approximately 300 km above the Earth's surface on the path between a satellite and a ground receiving station. Given that the orbital altitudes of GNSS satellites exceed this height by a factor of 60–80, the TEC values measured along the GNSS satellite–GNSS receiver path can be attributed to the ionospheric region located above the corresponding territory or water area over which the ray path is projected.

Fig. 2 illustrates an example of a GNSS receiver–GNSS satellite track for satellite G26 and receiver VLAD. The track shows the positions of

the corresponding GNSS receivers as well as the time of signal reception (UTC). Based on such tracks, it is possible to associate TEC measurements with specific geographic regions. For instance, TEC values projected over Japan correspond to the ionospheric layer above Japan at the corresponding time, while other track segments represent ionospheric conditions over adjacent areas.

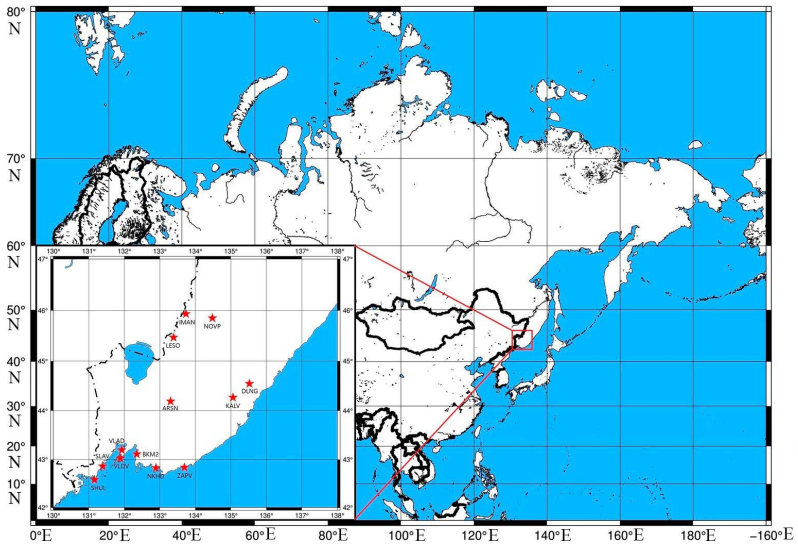

F i g. 1. Location of GNSS receivers in the Primorsky Territory. Station codes and corresponding locations: ARSN – Starosysoevka; BKM2 – Bolshoy Kamen; DLNG – Dalnegorsk; IMAN – Dalnerechensk; KALV – Kavalerovo; LESO – Lesozavodsk; NKHD – Nakhodka; NOVP – Novopokrovka; SHUL – Cape Shultz; SLAV – Slavyanka; VLAD – Vladivostok; VLDV – Russky Island; ZAPV – Zapovedny

In the example shown in Fig. 2, the maximum TEC values correspond to the ionospheric region above the Sea of Japan, located between the Primorsky Territory and the Japanese Islands and slightly closer to the Primorsky coast.

Thus, for each point along a given track, the total electron content of the ionospheric layer can be determined. By processing TEC data obtained over a specified time interval, it is possible to investigate the nature of perturbations in the ionosphere. Spectral analysis of selected observation time series allows the identification of dominant periods and amplitudes of pronounced spectral maxima, which may correspond either to propagating disturbances or to local variations in the TEC of a specific ionospheric region.

Processing of the GNSS signal to restore TEC values was performed using the methods described in [9, 10].

To determine the nature of detected oscillations, additional data obtained at different times but at approximately the same observation locations are required. If the periods of the identified oscillations are found to be consistent across independent data sets, they can be interpreted as eigenoscillations of the ionospheric electron layer. Otherwise, significant discrepancies in the oscillation periods indicate the presence of transient propagating disturbances that generate ionospheric waves with specific characteristic periods.

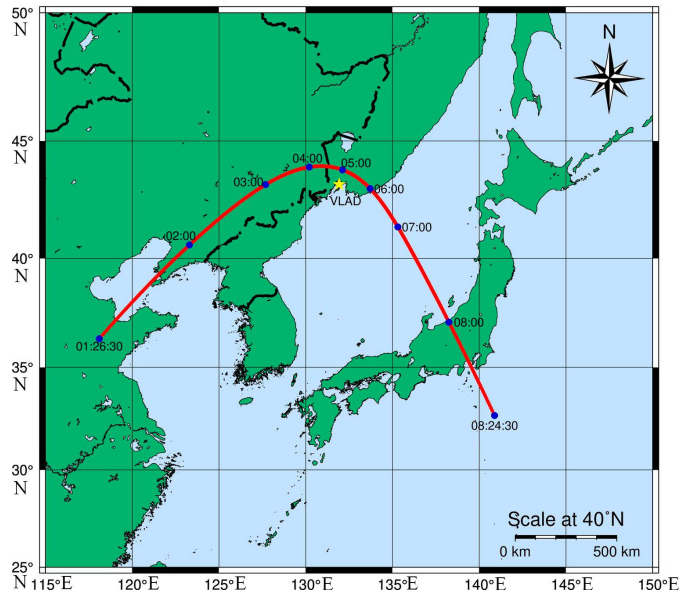

F i g. 2. GNSS receiver–GNSS satellite track for the VLAD–G26 pair. The red line indicates the ground projection of the signal path; markers denote GNSS receiver locations and the corresponding signal reception times (UTC)

The geomagnetic conditions during the volcanic event under study were classified as disturbed. Fig. 3 presents the temporal variation of the geomagnetic Kp index, derived from mid-latitude stations and characterizing global geomagnetic activity with a three-hour temporal resolution. As shown in Fig. 3, a moderate geomagnetic storm began on 14 January 2022, shortly before the onset of the eruptive episode, and caused ionospheric disturbances unrelated to the volcanic activity. These disturbances gradually weakened and persisted until 21 January 2022.

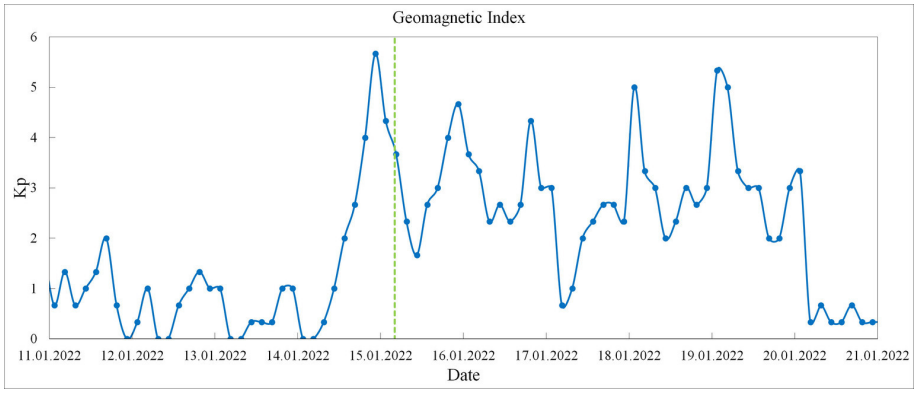

F i g. 3. Geomagnetic conditions during the considered time interval based on the Kp index (data from the GFZ Helmholtz Centre Potsdam [1]). The green vertical line marks the time of the volcano eruption

[1] GFZ. *Helmholtz Centre for Geosciences*. 2022. [online] Available at: https://www.gfz-potsdam.de/en/ [Accessed: 15 April 2022].

Another possible mechanism for the excitation of ionospheric oscillations is the propagation of an impulsive disturbance generated by the eruption of the Hunga Tonga–Hunga Ha'apai volcano through the atmosphere, followed by the excitation of oscillations in the hydrosphere, which were recorded by sea level measuring stations, as reported in [8]. That study analyzed sea level variations measured at specific locations in the Pacific Ocean and the Sea of Japan. Information on the level measuring stations was obtained from publicly available databases [2, 3].

Fig. 4 shows a map diagram of the location of level measuring stations. Experimental sea level data along the coast of Primorsky Territory were obtained using AANDERAA instruments equipped with hydrostatic pressure sensors with a measurement range of 0–10 m and an accuracy of ±0.2% of the full-scale range, with a sampling interval of 1 min. Measurements near the Japanese Islands were obtained using wave radar systems with the same temporal resolution.

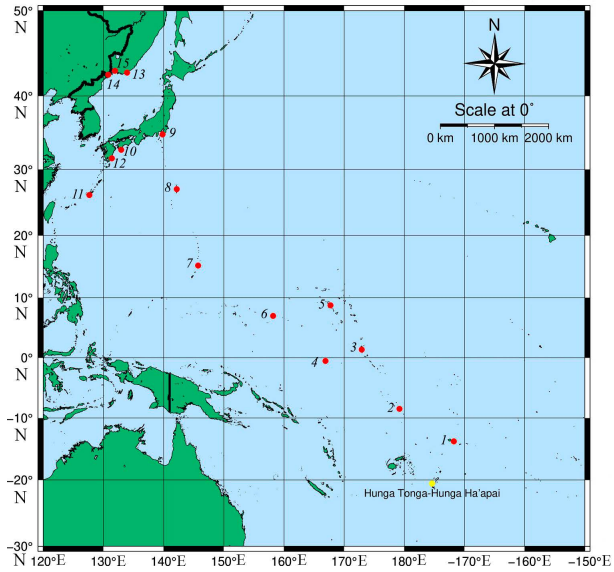

F i g. 4. Location of level measuring stations: *1–12* – stations in the Pacific Ocean; *13–15* – stations in the Sea of Japan near the coast of the Primorsky Territory of Russia

In this paper, GNSS-derived TEC data are available only for receivers located in the Primorsky Territory of Russia (see Fig. 1). However, the ground projections of GLONASS and GPS satellite tracks cover not only the Primorsky Territory but also the Korean Peninsula, the Japanese Islands, and the waters of the Sea of Japan, the Yellow Sea, and the Pacific Ocean washing the Japanese Islands.

Taking this into account, the analysis of sea level data from stations *9*, *10*, *12–15* was used to investigate the origin of the oscillations identified in the TEC spectra. To a lesser extent, data from stations *8* and *11* were also considered, provided that the satellite tracks passed over or in close proximity to these locations.

[2] Sea Level Station Monitoring Facility. 2022. [online] Available at: http://www.ioc-sealevelmonitoring.org/map.php [Accessed: 20 January 2022].

[3] Russian Tsunami Warning System. 2022. [online] Available at: http://www.rtws.ru/sea-level/ [Accessed: 20 January 2022].

When analyzing TEC variations above or near a specific level measuring station, the time series length was selected to be as short as possible in order to attribute the detected oscillations to a specific region. However, shorter time series result in reduced frequency resolution. Therefore, a compromise between time series length and frequency resolution was required.

The minimum length of the analyzed time series was set to 128 data points, providing a frequency resolution of $1/(127T)$ when using the periodogram method, where T is the sampling interval. To improve frequency resolution, the time series were additionally processed using the maximum likelihood estimation (MLE) method with 60 harmonics, approximately corresponding to the number of harmonics identified in the periodogram analysis.

MLE is a statistical method for estimating unknown parameters by maximizing the likelihood function [11]. It is based on the assumption that all information about a statistical sample is contained in the likelihood function. MLE is a popular statistical method that is used to create a statistical model based on data and to provide estimates of model parameters. Using the MLE method for a fixed data set and a basic probabilistic model, the values of the model parameters that make the information "closer" to the real data can be obtained. MLE provides a unique and simple way to identify solutions in the case of normal distribution.

The results obtained from the processing of sea level data from stations *8–15* are summarized in Table 1.

Table 1

Periods obtained from data from level measuring stations

Station Number	Name	Periods [8]	
		Background	Signal
8	Chichijima	20 min 28.0 s 16 min 30.3 s 13 min 49.7 s	20 min 28.0 s 15 min 02.9 s 12 min 47.5 s
9	Mera	6 min 09.9 s 5 min 19.8 s 22 min 14.7 s	22 min 14.7 s 6 min 05.5 s 6 min 38.7 s
10	Tosashimizu	20 min 28.0 s 39 min 21.4 s	20 min 28.0 s 24 min 21.8 s 42 min 38.2 s
11	Naha	26 min 55.7 s	24 min 21.8 s 10 min 26.5 s 22 min 14.7 s 25 min 34.9 s 19 min 40.7 s
12	Aburatsu	26 min 55.7 s 17 min 38.6 s 11 min 37.7 s	22 min 14.7 s 10 min 26.5 s 9 min 18.2 s
13	Preobrazheniye	31 min 58.7 s 15 min 59.3 s	30 min 05.8 s 9 min 28.5 s 15 min 59.3 s
14	Pos'et	31 min 58.7 s 17 min 38.6 s 10 min 53.2 s	30 min 05.8 s 17 min 38.6 s 11 min 22.2 s
15	Vladivostok	39 min 21.4 s 31 min 58.7 s	31 min 58.7 s

Given that the propagation speed of the perturbation generated by the volcanic explosion toward individual level measuring stations is slightly lower than the speed of sound in air, it can be assumed that sea level oscillations recorded at each station were primarily excited by atmospheric pressure variations induced by a passage of the volcanic pressure pulse. At the same time, the possibility of direct excitation of sea level oscillations by the passing impulse itself cannot be excluded.

Thus, two main mechanisms for the excitation of water surface oscillations recorded by the level measuring stations can be considered: 1) excitation by natural oscillations of the atmospheric region above a given station, and 2) excitation of eigenoscillations of the Pacific Ocean basin (e.g., seiches) triggered by the propagating atmospheric impulse.

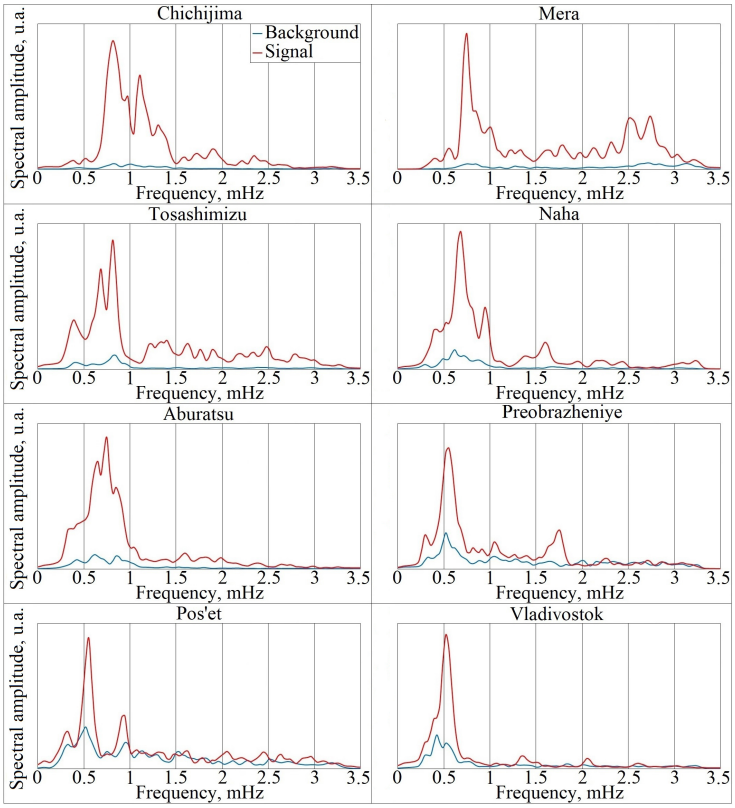

F i g. 5. Spectral characteristics of sea level variations recorded at level measuring stations *8–15*. The red curve represents the signal spectrum, and the blue curve corresponds to the background spectrum

For clarity, the oscillation periods listed in Table 1 are presented in the form of spectra in Fig. 5, where the red curve represents the signal spectrum and the blue curve corresponds to the background spectrum. As the atmospheric pressure pulse propagated over the Pacific Ocean, it excited local oscillations of water masses (seiches) specific to the regions where the level measuring stations were located. In addition to regional oscillations, seiches of the Sea of Japan were observed within

the period range of 30 min 05.8 s to 31 min 58.7 s at all stations located in the Sea of Japan.

If, during the processing of TEC time series segments along GNSS satellite tracks above or near specific level measuring stations, oscillation periods are identified that approximately coincide with those obtained from sea level records, it can be concluded that, in both cases, the source of the identified oscillations is associated with atmospheric regions located above or near the corresponding stations listed in Table 1.

Accordingly, the problem addressed in this study can be formulated as follows: 1) to process segments of GNSS-derived TEC data along GNSS receiver–GNSS satellite tracks in the vicinity of selected level measuring stations; 2) to compare the obtained spectral characteristics with the results presented in Table 1; 3) to perform a physical interpretation of the identified oscillations.

Results

This section presents the results of processing and analysis of GNSS-derived TEC recordings obtained for various receiver–satellite pairs over selected time intervals. Table 2 summarizes the TEC data used in the analysis, including the specific GNSS receiver–satellite combinations and the maximum length of the time series suitable for processing. Due to the limited duration of the available records, oscillations with period longer than 1 h could not be reliably identified. Nevertheless, the obtained results provide sufficient information to draw conclusions regarding the origin of the oscillations detected in both TEC records and sea level measurements. Prior to the analysis, it should be noted that all recordings have the same sampling frequency of approximately 0.033 Hz, corresponding to a sampling interval of 30 s.

All TEC time series were processed to identify the dominant oscillatory processes present in each record. Spectral analysis was performed using two different methods: the periodogram method and the MLE method. In the MLE analysis, the number of harmonics was set to 60. TEC is given in TECU (Total Electron Content Units). Several recordings exhibited pronounced spectral peaks characteristic of specific regions. Fig. 6 shows the TEC time series obtained for the ARSN receiver–G08 satellite pair. Pronounced low-frequency oscillations are clearly visible in the record even prior to spectral analysis.

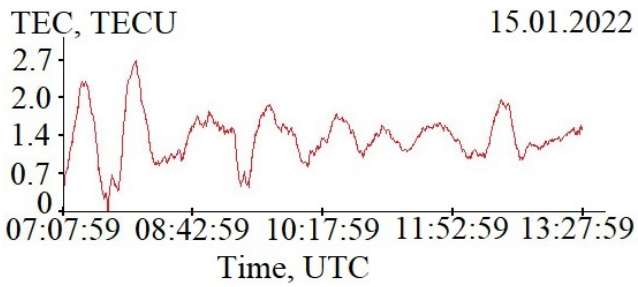

F i g. 6. Temporal variation of TEC derived from GNSS observations on 15 January 2022

Table 2

Information about GNSS-data

Receiver – Satellite	Date, time interval	Duration, s	GNSS Receiver – Satellite	Date, time interval	Duration, s
ARSN – R22	15.01.2022 07:00:29.0–11:46:29.0	17100	VLAD – G31	15.01.2022 01:26:30.0–08:25:00.0	25080
BKM2 – R22	15.01.2022 07:26:29.0–11:36:59.9	15000	ARSN – G27	15.01.2022 06:06:59.0–11:56:59.0	20940
KALVR – R22	15.01.2022 07:05:29.0–11:45:29.0	16740	BKM2 – G27	15.01.2022 05:35:29.0–12:17:29.0	24060
SLAV – R22	15.01.2022 06:59:29.0–11:33:29.0	16380	IMAN – G27	15.01.2022 05:52:29.0–12:17:59.0	23100
IMAN – R22	15.01.2022 07:36:29.0–11:58:59.0	15780	ARSN – G26	15.01.2022 03:33:59.0–09:38:29.0	21840
VLAD –R22	15.01.2022 07:25:29.0–11:43:29.0	15420	BKM2 – G26	15.01.2022 03:04:29.0–08:43:59.0	20340
ARSN – R21	15.01.2022 06:02:29.0–10:07:29.0	14640	SHUL – G26	15.01.2022 03:15:29.0–09:31:59.0	22560
KALVR – R21	15.01.2022 05:38:29.0–10:12:29.0	16380	SLAV – G26	15.01.2022 03:16:59.0–10:04:59.0	24420
SLAV – R21	15.01.2022 05:36:29.0–10:19:59.0	16980	VLAD – G26	15.01.2022 02:58:59.0–09:56:59.0	25020
VLAD –R21	15.01.2022 05:39:59.0–10:13:59.0	16380	ZAPV – G26	15.01.2022 03:06:29.0–09:58:59.0	24720
ZAPV – R21	15.01.2022 05:36:29.0–10:15:29.0	16680	ARSN – G16	15.01.2022 04:59:59.0–11:11:59.0	22260
ARSN – R12	15.01.2022 06:21:29.0–11:30:59.0	18540	BKM2 – G16	15.01.2022 04:17:59.0–11:28:29.0	25800
BKM2 – R12	15.01.2022 05:53:29.0–11:55:29.0	21660	KALVR – G16	15.01.2022 04:50:29.0–11:13:59.0	22980
IMAN – R12	15.01.2022 06:06:59.0–11:47:29.0	20400	SHUL – G16	15.01.2022 04:42:29.0–11:01:29.0	22680
VLAD – R12	15.01.2022 06:03:29.0–11:54:59.0	21060	SLAV – G16	15.01.2022 04:40:59.0–11:12:59.0	23460
KALVR – R11	15.01.2022 03:49:59.0–10:12:29.0	22920	VLAD – G16	15.01.2022 04:23:29.0–11:25:29.0	25260
SLAV – R11	15.01.2022 03:39:29.0–10:18:29.0	23940	ZAPV – G16	15.01.2022 04:37:59.0–11:22:59.0	24240
ZAPV – R11	15.01.2022 03:49:29.0–10:09:59.0	22800	ARSN – G08	15.01.2022 07:07:59.0–13:27:59.0	22740
ARSN – G31	15.01.2022 02:07:29.0–08:08:29.0	21600	IMAN – G08	15.01.2022 06:56:29.0–13:45:29.0	24480
BKM2 – G31	15.01.2022 01:47:00.0–08:22:00.0	23640			

Fig. 7 presents the corresponding spectral estimates: Fig. 7, a shows the spectrum obtained using the periodogram method with three averages, while Fig. 7, *b* shows the spectrum derived using the MLE method with 60 harmonics. The periodogram spectrum (Fig. 7, *a*) contains a dominant peak with a period of 46 min 32.7 s. In contrast, the MLE spectrum (Fig. 7, *b*) resolves two pronounced peaks with periods of 30 min 27.8 s (A = 0.79 TECU) and 46 min 20.4 s (A = 0.77 TECU). In addition, a weaker peak with a period of 11 min 01.4 s (A = 0.09 TECU) is also observed.

The ground projection of the ARSN receiver–G08 satellite track is shown in Fig. 8. This track passes over level measuring stations *13*, *14*, and *15* (see Fig. 4), whose sea level spectra exhibit strong components in the period range of 30–32 min. Therefore, the spectral peak with a period of 30 min 27.8 s identified in the TEC data for the ARSN receiver–G08 satellite pair can be reasonably attributed to the same origin as the corresponding oscillations observed in the sea level records.

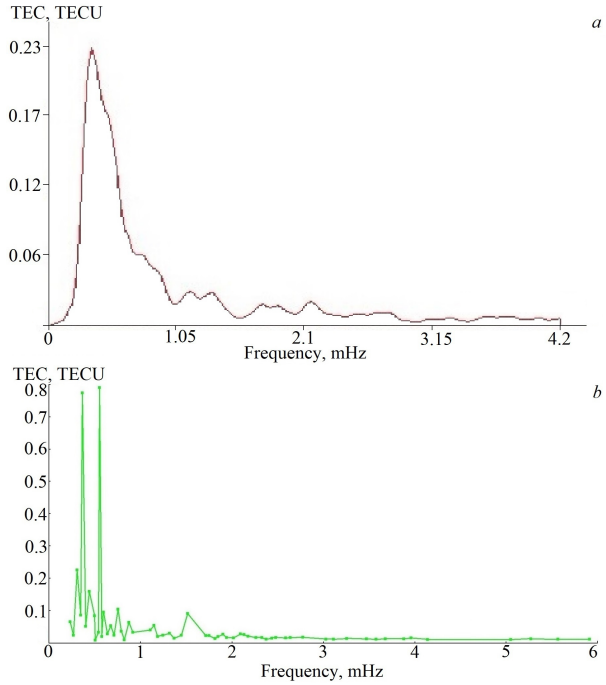

F i g. 7. Spectrum obtained by processing the series shown in figure 6 using the periodogram method (*a*) and the maximum likelihood estimation method (*b*)

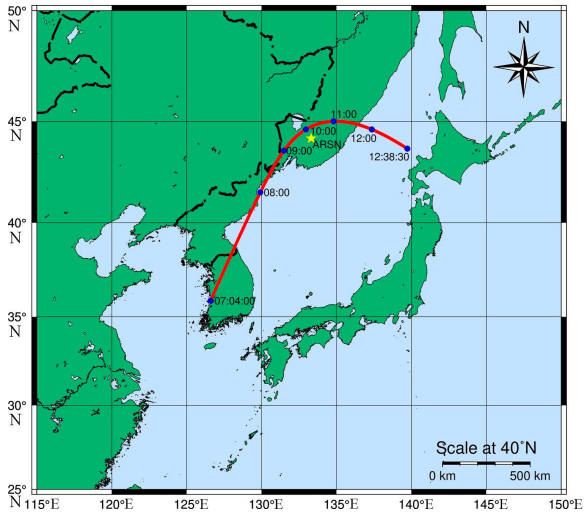

F i g. 8. Track ARSN receiver–G08 satellite (red line)

Let us consider another track of the IMAN receiver–R12 satellite, shown in Fig. 9. The track passes over receiving stations *13* and *15*, crosses the Sea of Japan, and ends not far from sea level station *10*.

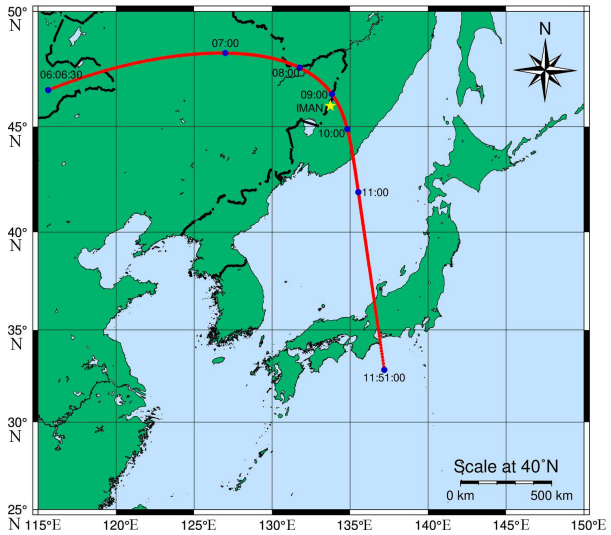

F i g. 9. Track IMAN receiver–R12 satellite (red line)

Spectral processing of the entire data series using the MLE method produced the spectrum shown in Fig. 10. The dominant peak corresponds to a period of 42 min 14.6 s (A = 0.63 TECU), which is close to the oscillation period identified in the record of level measuring station *10*. Two other significant peaks, with periods of 34 min 18.8 s (A = 0.38 TECU) and 31 min 08.0 s (A = 0.27 TECU), are close to the periods identified in the record of level measuring station *15*. The remaining significant peaks in the spectrum also correspond to maxima identified during the processing of records from stations *10* and *15*.

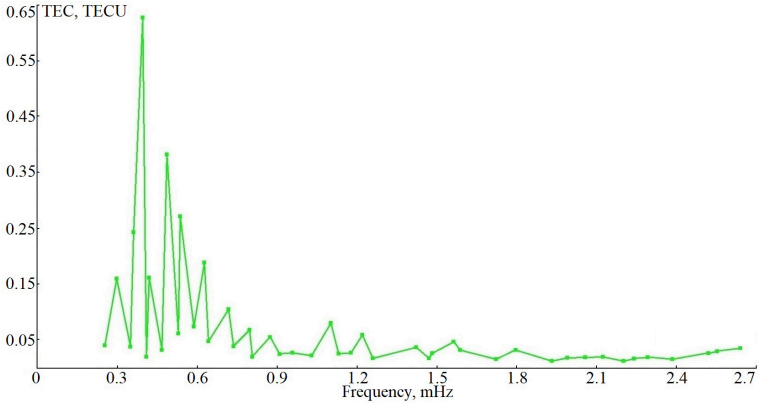

F i g. 10. Spectrum obtained by processing the entire data series of the IMAN receiver–R12 satellite track by the MLE method

When a shorter segment of the series – from the Primorsky Territory to the end of the tack – is analyzed, spectral processing using the MLE method reveals pronounced peaks with periods of 42 min 38.2 s, 32 min 33.0 s, and 25 min 59.2 s. These periods are close to those identified in the records of level measuring stations *10*, *15* and *13*, respectively.

Fig. 11 shows another track of the BKM2 receiver–G31 satellite. The track passes over level measuring station *14*, crosses the Sea of Japan and the Japanese Islands, and ends between level measuring stations *10* and *9*. In this case, the data file was divided into two segments. The first segment contains 256 points and spans the interval from 04 h 32 min 00.0 s to 06 h 40 min 30.0 s, while the second segment contains 128 points and covers the interval from 07 h 17 min 30 s to 08 h 22 min 00.0 s. Each segment was processed using the MLE method with 60 harmonics.

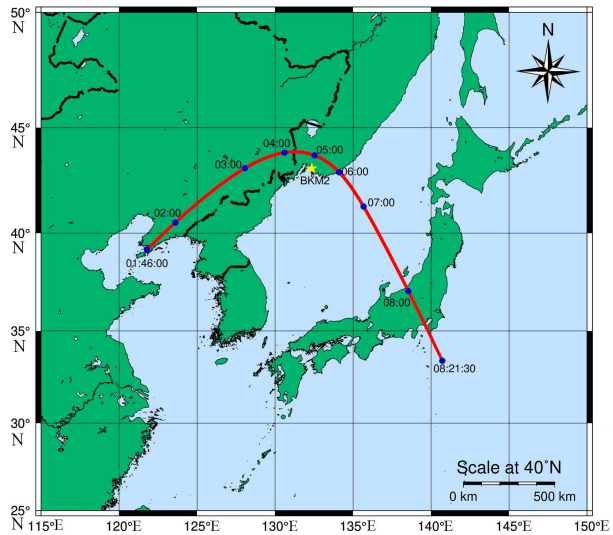

F i g. 11. Track BKM2 receiver – G31 satellite (red line)

Figure 12, a shows the spectrum obtained from processing the first segment of the TEC record in the vicinity of level measuring station *14*, whereas Fig. 12, *b* presents the spectrum derived from the second segment near level measuring stations *10* and *9*. As shown in Fig. 12, *a*, pronounced spectral maxima are observed at periods of 17 min 53.8 s (A = 0.24 TECU), 11 min 33.4 s (A = 0.017 TECU), 30 min 40.6 s (A = 0.08 TECU), 10 min 50.4 s (A = 0.08 TECU). These periods are close to those of the maxima identified during processing of the data from level measuring station *14*. Fig. 12, *b* reveals significant maxima at periods of 59 min 34.6 s (A = 0.23 TECU), 25 min 44.5 s (A = 0.18 TECU), 07 min 58.2 s (A = 0.10 TECU), which correspond to the maxima detected in the records of level measuring stations *10* and *9*.

In concluding this chapter, we consider another track of the BKM2 receiver–G27 satellite, shown in Fig. 13. The track passes over level measuring station *11*, runs near station *12* along the Korean Peninsula, reaches level measuring station *14*,

and then continues eastward over the Sea of Japan, exiting between the Japanese Islands and Sakhalin Island.

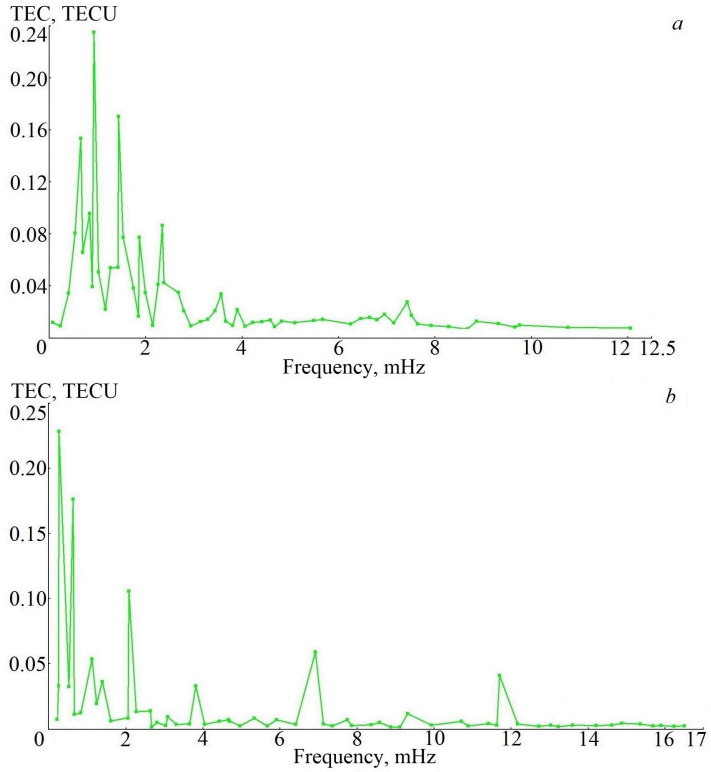

F i g. 12. Spectrum obtained from processing the first (*a*) and second (*b*) sections of the BKM2 receiver–G31 satellite track data

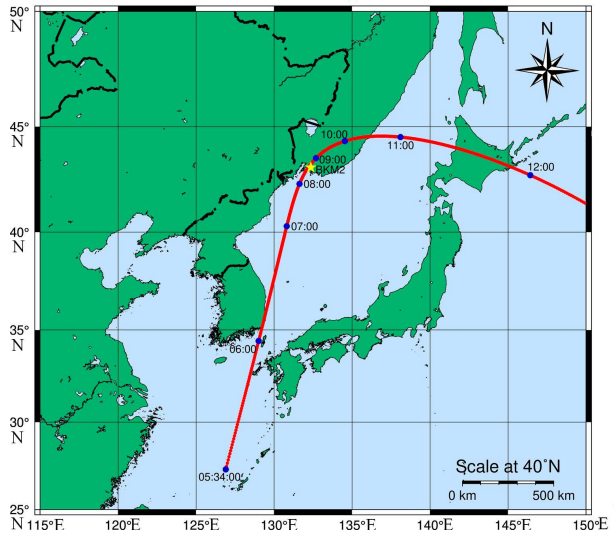

F i g. 13. Track BKM2 receiver–G27 satellite (red line)

Spectral processing of the first segment of the data, consisting of 128 points, was performed using the MLE method with 60 harmonics. The resulting spectrum is shown in Fig. 14, *a*. Pronounced maxima are observed at periods of 39 min 56.6 s (A = 1.16 TECU), 11 min 53.5 s (A = 1.12 TECU), and 19 min 08.9 s (A = 0.49 TECU). These periods are close to those of the maxima identified during processing of data from level measuring stations *10*, *12* and *11*, respectively. Fig. 14, *b* presents the spectrum obtained from processing the second segment of the BKM2 receiver– G27 satellite track, also with a length of 128 points. In this spectrum, significant maxima are detected at periods of 44 min 22.5 s (A = 0.54 TECU), 17 min 11.6 s (A = 0.19 TECU), and 11 min 23.0 s (A=0.11 TECU), which correspond to the maxima identified in the records of level measuring station *14*.

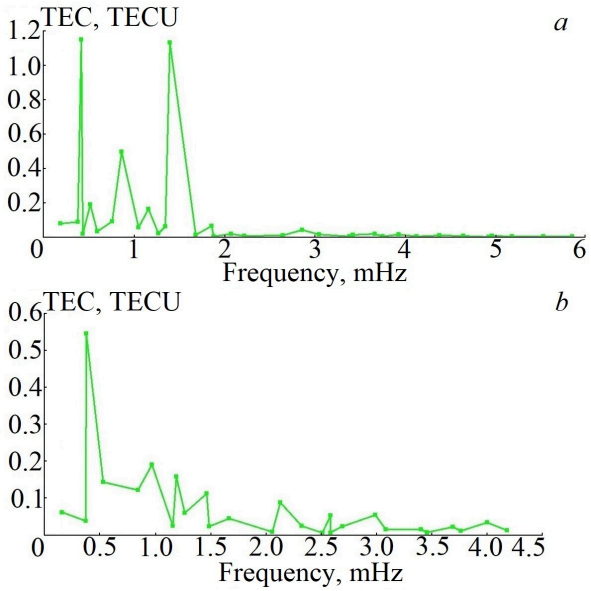

F i g. 14. Spectrum obtained from processing the first (*a*) and second (*b*) sections of the BKM2 receiver–G27 satellite track data

We investigated several cases from the complete data set listed in Table 2. Generalized information on the results obtained from processing the primary GNSS receiver–GNSS satellite data is presented in the Appendix. The Appendix summarizes periods of the selected TEC oscillations as well as their percentage agreement with the periods of dominant peaks identified during processing of records from level measuring stations.

Each column of the table sequentially presents the following parameters: the time interval of the processed data segment; the name of the GNSS satellite; the period of the selected maximum; and, in parentheses, the period of the corresponding maximum identified in the record of the level measuring station with its percentage deviation from the period of the selected maximum in the GNSS receiver–GNSS satellite data segment. As expected, limited data were obtained for

level measuring stations *8*, *11*, *12*. For the remaining stations, a good agreement is observed, with the maximum single deviation not exceeding 19.9% for level measuring station *9*. On average, the deviation for level measuring stations *9*, *10*, and *13–15* is 2.5%.

Conclusions

Analysis of ionospheric TEC variations derived from GNSS observations along the GNSS receiver–GNSS satellite track demonstrates that the periods of the dominant spectral maxima are in good agreement with high accuracy. These periods coincide with those identified during processing of data from level measuring stations reported in [8], provided that the corresponding segments of the GNSS receiver–GNSS satellite track are located near a given level measuring station.

The obtained results indicate that the oscillation periods indicated in this study and in [8] correspond to the same eigen atmospheric oscillations over specific territories and water areas. Excitation of these oscillations by various powerful impulsive sources propagating in the atmosphere can lead not only to the development of atmospheric wave activity but also to the generation of meteotsunamis [12] in individual bays, provided that the periods of the atmospheric eigen oscillations are close to the natural seiche periods of these bays.

In addition, atmospheric eigen oscillations may be excited by individual tones and overtones of the Earth's normal modes [13]. Taking into account the impedances of the interacting media, the opposite effect may also occur, namely, the transfer of energy from atmospheric eigenmodes to individual tones and overtones of the Earth's eigen oscillations during resonant or near-resonant nonlinear interaction.

Further investigation of these processes is of considerable interest and will be a focus of further studies involving integrated experiments with modern laser interferometric systems capable of measuring deep infrasound signals with picolevel accuracy [14, 15].

REFERENCES

1. Calais, E. and Minster, J.B., 1995. GPS Detection of Ionospheric Perturbations Following the January 17, 1994, Northridge Earthquake. *Geophysical Research Letters*, 22(9), pp. 1045–1048. https://doi.org/10.1029/95GL00168
2. Heki, K. and Ping, J., 2005. Directivity and Apparent Velocity of the Coseismic Ionospheric Disturbances Observed with a Dense GPS Array. *Earth and Planetary Science Letters*, 236(3–4), pp. 845–855. https://doi.org/10.1016/j.epsl.2005.06.010
3. Tsugawa, T., Saito, A., Otsuka, Y., Nishioka, M., Maruyama, T., Kato, H., Nagatsuma, T. and Murata, K.T., 2011. Ionospheric Disturbances Detected by GPS Total Electron Content Observation after the 2011 off the Pacific Coast of Tohoku Earthquake. *Earth, Planets and Space*, 63(7), 66. https://doi.org/10.5047/eps.2011.06.035
4. Jin, S., Jin, R. and Li, D., 2017. GPS Detection of Ionospheric Rayleigh Wave and Its Source Following the 2012 Haida Gwaii Earthquake. *Journal of Geophysical Research: Space Physics*, 122(1), pp. 1360-1372. https://doi.org/10.1002/2016JA023727
5. Grawe, M.A. and Makela, J.J., 2015. The Ionospheric Responses to the 2011 Tohoku, 2012 Haida Gwaii, and 2010 Chile Tsunamis: Effects of Tsunami Orientation and Observation Geometry. *Earth and Space Science*, 2(11), pp. 472-483. https://doi.org/10.1002/2015EA000132
6. Adam, D., 2022. Tonga Volcano Eruption Created Puzzling Ripples in Earth's Atmosphere. *Nature*, 601, 497. https://doi.org/10.1038/d41586-022-00127-1
7. Carpenter, E.W., Harwood, G. and Whiteside, T., 1961. Microbarograph Records from the Russian Large Nuclear Explosions. *Nature*, 192(4805), 857. https://doi.org/10.1038/192857a0

8. Dolgikh, G.I., Dolgikh, S.G. and Ovcharenko, V.V., 2022. Initiation of Infrasonic Geosphere Waves Caused by Explosive Eruption of Hunga Tonga-Hunga Ha'apai Volcano. *Journal of Marine Science and Engineering*, 10(8), 1061. https://doi.org/10.3390/jmse10081061

9. Astafyeva, E., 2019. Ionospheric Detection of Natural Hazards. *Reviews of Geophysics*, 57(4), pp. 1265-1288. https://doi.org/10.1029/2019RG000668

10. Hofmann-Wellenhof, B., Lichtenegger, H. and Wasle, E., 2008. *GNSS - Global Navigation Satellite Systems*. Vienna, New York: Springer, 518 p. https://doi.org/10.1007/978-3-211-73017-1

11. Rossi, R.J., 2018. *Mathematical Statistics: An Introduction to Likelihood Based Inference*. New York: John Wiley & Sons, 448 p.

12. Rabinovich, A.B., Šepić, J., Medvedev, I.P. and Tomson, R.E., 2025. A Triple Jeopardy Flood Event: Coincident Arrival of the 2022 Tonga Tsunami with a Storm Surge and Meteotsunami on the East Coast of the United States. *Bulletin of the American Meteorological Society*, 106(2), pp. E290–E309. https://doi.org/10.1175/BAMS-D-24-0040.1

13. Shved, G.M., Ermolenko, S.I., Karpova, N.V., Wendt, S. and Jacobi Ch., 2013. Detecting Global Atmospheric Oscillations by Seismic Instruments. *Izvestiya, Physics of the Solid Earth*, 49(2), pp. 278–288. https://doi.org/10.1134/S1069351313010138

14. Dolgikh, G.I., 2011. Principles of the Designing Single-Coordinate Laser Strainmeters. *Technical Physics Letters*, 37(3), pp. 204–206. https://doi.org/10.1134/S1063785011030035

15. Dolgikh, G.I., Budrin, S.S., Dolgikh, S.G. and Plotnikov, A.A., 2020. Supersensitive Detector of Hydrosphere Pressure Variations. *Sensors*, 20(23), 6998. https://doi.org/10.3390/s20236998

Submitted 31.07.2025; approved after review 21.10.2025;
accepted for publication 10.11.2025.

About the authors:

Grigoriy I. Dolgikh, Academician of RAS, V.I. Il'ichev Pacific Oceanological Institute, Far Eastern Branch of Russian Academy of Sciences (43 Baltiyskaya Str., Vladivostok, 690041, Russian Federation), DSc. (Phys.-Math.), Professor, **ORCID ID: 0000-0002-2806-3834**, **Scopus Author ID: 7003888822**, **SPIN-code: 5241-3375, Web of Science ResearcherID: A-7685-2014**, dolgikh@poi.dvo.ru

Mikhail A. Bolsunovskii, Graduate Student, V.I. Il'ichev Pacific Oceanological Institute, Far Eastern Branch of Russian Academy of Sciences (43 Baltiyskaya Str., Vladivostok, 690041, Russian Federation), **ORCID ID: 0000-0002-9197-7452**, **Scopus Author ID: 58405940300**, **SPIN-code: 8711-4746**, **Web of Science ResearcherID: HMO-8458-2023**, bolsunovsky.ma@poi.dvo.ru

Stanislav G. Dolgikh, Head of the Laboratory of Nonlinear Hydrophysics and Natural Disasters, V.I. Il'ichev Pacific Oceanological Institute, Far Eastern Branch of Russian Academy of Sciences (43 Baltiyskaya Str., Vladivostok, 690041, Russian Federation), DSc. (Tech.), **ORCID ID: 0000-0001-9828-5929**, **Scopus Author ID: 6604069353**, **SPIN-code: 1836-2541**, sdolgikh@poi.dvo.ru

Contribution of the co-authors:

Grigoriy I. Dolgikh – statement of study aims and objectives, qualitative analysis of the results and interpretation thereof, discussion of the study results, preparation of the manuscript

Mikhail A. Bolsunovskii – statement of study aims and objectives, data processing analysis of the results, interpretation thereof and visualization, drawing conclusions, preparation of the manuscript

Stanislav G. Dolgikh – discussion of the study results, data visualization, preparation of the manuscript

The authors have read and approved the final manuscript.
The authors declare that they have no conflict of interest.

Appendix
Summary of TEC oscillation periods for selected satellites and their agreement with water-level measuring stations

Station No.	ARSN – satellite	BKM2 – satellite	KALV – satellite	SLAV – satellite	VLAD – satellite	SHUL – satellite	ZAPV – satellite	IMAN-satellite
8	–	–	05:39-06:43 R21 14:03.2 (13:49.7 1.6%) 18:17.7 (20:28.0 10.6%)	–	–	–	–	–
9	07:04-08:09 G31 06:42.4 (06:38.7, 0.9%)	07:18-08:22 G31 07:58.2 (06:38.7 19.9%)	06:43-7:47 R21 22:03.1 (22:14.7 0.9%) 05:59.6 (06:05.5 1.6%)	06:39-08:48 R11 22:47.4 (22:14.7 2.4%) 21:46.9 (22:14.7 2.1%)	05:40-09:57 G26 21:36.3 (22:14.7 2.9%)	09:38-10:44 G16 21:57.7 (22:14.7 1.3%)	05:36-10:17 R21 22:01.5 (22:14.7 1.0%) 06:40-08:49 R21 04:50.8 (5:19.8 9.1%) 22:11-23:16 R21 22:23.5 (22:14.7 0.7%) 06:31-09:54 G26 22:49.3 (22:14.7 2.6%)	–
10	7:00-8:05 R12 19:57.7 (20:28.0 2.4%) 07:04-08:09 G31 41:23.4 (42:38.2 4.7%) 20:15.9 (20:28.0 1.0%) 07:04-08:09 G31 20:15.9 (20:28.0 1.0%)	10:51-11:56 R12 19:06.2 (20:28.0 6.7%) 05:36-06:40 G27 39:56.6 (39:21.4 1.5%) 06:34-07:39 G27 44:22.5 (42:38.2 4.1%) 04:18-05:23 G16 44:22.5 (42:38.2 4.1%)	–	07:00-11:34 R22 42:43.0 (42:38.2 0.2%) 06:40-07:45 R21 24:42.5 (24:21.8 1.4%) 06:39-08:48 R11 41:39.6 (42:38.2 2.3%)	05:40-06:45 R21 20:29.9 (20:28.0 0.2%) 08:03-11:54 R12 38:36.6 (39:21.4 1.9%) 05:32-07:41 G31 19:41.4 (20:28.0 3.8%) 05:45-12:14 G27 43:11.5 (42:38.2 1.3%) 21:24.7 (20:28.0 4.6%)	–	06:40-08:49 R21 43:21.2 (42:38.2 1.7%) 03:31-04:37 G26 41:56.0 (42:38.2 1.7%) 19:02.1 (20:28.0 7.0%) 03:47-08:04 G26 19:09.6 (20:28.0 6.4%)	08:06-11:48 R12 42:38.2 (42:38.2 0.0%) 06:06-11:48 R12 42:14.6 (42:38.2 0.9%) 05:52-06:57 R27 19:50.2 (20:28.0 3.1%)
11	–	05:36-06:40 G27 19:08.9 (19:40.7 2.7%)	–	–	–	–	–	–
12	–	05:36- 06:40 G27 11:53.5c (11:37.7 2.3%)	–	–	05:45- 06:50 G27 22:21.6 (22:14.7 0.5%) 10:17.5 (10:26.5 1.4%)	–	03:31- 04:37 G26 21:59.5 (22:14.7 1.1%)	–

Table continued

Station No.	ARSN – satellite	BKM2 – satellite	KALV – satellite	SLAV – satellite	VLAD – satellite	SHUL – satellite	ZAPV – satellite	IMAN- satellite
13	09:09-10:13 R22 09:09.3 (09:28.5 3.4%) 07:07-09:15 R21 09:28.0 (09:28.5 0.1%) 08:20-11:31 R12 30:45.8 (30:05.8 2.2%) 06:07-07:13 G27 09:09.3 (09:28.5 3.4%) 07:00-09:09 G26 16:15.6 (15:59.3 1.7%) 09:00-10:05 G08 09:04.0 (09:28.5 4.3%)	07:51-08:56 R12 29:55.9 (30:05.8 0.5%)	05:46-06:51 G16 15:20.8 (15:59.3 4.0%) 10:03-11:08 G16 30:51.3 (30:05.8 2.5%)	06:40-07:45 R21 09:43.0 (09:28.5 2.6%) 05:36-10:20 R21 31:44.9 (31:58.7 0.7%) 07:38-08:44 G16 16:12.1 (15:59.3 1.3%)	07:26-08:24 R22 09:14.4 (09:28.5 2.5%) 15:23.5 (15:59.3 3.7%) 05:40-06:45 R21 15:35.2 (15:59.3 2.5%) 09:13.8 (09:28.5 2.6%) 05:39-10:14 R21 30:54.1 (30:05.5 2.7%) 22:15-23:42 R21 15:56.6 (15:59.3 0.3%) 05:32-07:41 G31 15:36.1 (15:59.3 2.4%) 06:33-08:42 G16 09:46.1 (09:28.5 3.1%) 10:20-11:26 G16 09:45.9 (09:28.5 3.1%)	04:32-05:37 G26 09:09.6 (09:28.5 3.3%) 15:19.0 (15:59.3 4.2%) 05:32-06:37 G26 09:01.0 (09:28.5 4.8%) 06:42-07:47 G16 09:04.7 (09:28.5 4.2%)	22:11-23:16 R21 15:58.5 (15:59.3 0.1%) 06:49-07:54 R11 09:09.0 (09:28.5 3.4%) 05:43-07:51 G16 30:35.4 (30:05.8 1.6%) 09:03.6 09:49.5 (09:28.5 4.4%, 3.7%)	07:36-11:59 R22 31:46.7 (31:58.7 0.6%) 05:52-12:18 G27 30:26.3 (30:05.8 1.1%) 11:37-13:46 G08 09:54.0 (09:28.5 4.5%)
14	06:03-07:07 R21 17:05:0 (17:38.6 3.2%) 08:20-10:29 R12 18:00.4 (17:38.6 2.1%) 08:20-11:31 R12 30:45.8 (30:05.8 2.2%) 07:08-08:13 G08 16:51.0 (17:38.6 4.5%) 08:00-09:05 G08 30.09.4 (30:05.8 0.2%)	09:56-11:00 R22 17:50.8 (17:38.6 1.2%) 09:52-10:56 R22 17:27.4 (17:38.6 1.0%) 07:51-10:00 R12 17:53.2 (17:38.6 1.4%) 04:32-06:41 G31 10:50.4 (10:53.2 0.4%) 06:34-07:39 G27 17:11.6 (17:38.6 2.6%) 11:23.0 (11:22.2 0.1%) 05:35-12:18 G27 17:21.3 (17:38.6 1.6%) 11:49.7 (11:22.2 4.0%) 06:31-07:37 G26 17:40.1 (17:38.6 0.1%) 10:26.0 (10:53.2 4.2%) 06:12-07:17 G16 11:07.3 (11:22.2 2.2%)	05:46-06:51 G16 10:35.1 (10:53.2 2.8%) 06:46-07:51 G16 17:25.1 (17:38.6 1.3%)	05:36-10:20 R21 31:44.9 (31:58.7 0.7%) 03:32-04:37 G26 10:41.9 (10:53.2 1.7%) 04:32-05:37 G26 11:00.9 (10:53.2 1.2%)	07:26-11:44 R22 11:02.1 (10:53.2 1.4%) 06:44-07:49 R21 11:05.9 (10:53.2 1.9%) 22:15-23:20 R21 11:32.4 (11:22.2 1.5%) 08:03-10:12 R12 17:07.6 (17.38.6 2.9%) 11:55.0 (11:22.2 4.8%) 06:45-08:54 G27 11:36.1 (11:22.2 2.0%) 05:45-12:14 G27 18:02.8 (17:38.6 2.3%) 05:40-09:57 G26 17:04.5 (17:38.6 3.2%) 10:20-11:26 G16 17:54.4 (17:38.6 1.5%)	03:32-04:35 G26 10:44.0 (10:53.2 1.4%)	04:32-06:41 G26 17:01.2 (17:38.6 3.5%) 05:43-07:51 G16 30:35.4 (30:05.8 1.6%) 11:13.9 (11:22.2 1.2%)	07:36-11:59 R22 17:02.0 (17:38.6 3.5%) 05:52-12:18 G27 30:26.3 (30:05.8 1.1%) 06:57-08:01 G08 17:36.6 (17:38.6 0,2%)

Table concluded

Station No.	ARSN – satellite	BKM2 – satellite	KALV – satellite	SLAV – satellite	VLAD – satellite	SHUL – satellite	ZAPV – satellite	IMAN-satellite
15	08:20-09:25 R12 39:44.7 (39:21.4 1.0%) 29:35.9 (31:58.7 7.4%) 08:20-10:29 R12 41:29.9 (39:21.4 5.4%) 08:20-11:31 R12 40:44.4 (39:21.4 3.5%) 06:48-11:05 G16 40:01.1 (39:21.4 1.7%) 32:32.0 (31:58.7 1.7%) 08:20-09:25 R12 29:35.9 (31:58.7 7.4%)	07:51-10:00 R12 40:02.6 (39:21.4 1.7%) 05:12-06:17 G16 39:38.8 (39:21.4 0,7%) 10:56.4 (10:53.2 0.5%)	05:46-06:51 G16 39:33.0 (39:21.4 0.5%)	06:39-07:44 G16 30:51.3 31:28.6 (31:58.7 3.5%)	–	05:41-06:47 G16 29:39.2 (31:58.7 7.2%)	05:43-07:51 G16 30:35.4 (31:58.7 4.3%)	06:24-08:33 G27 31:31.4 (31:58.7 1.4%) 08:56-10:01 G08 31:59.1 (31:58.7 0.0%)

Note. For each GNSS receiver–satellite data segment, the table reports time of the processed section of the record; constellations (R – GLONASS, G – GPS) and number of the GNSS satellite; period of the selected maximum; in brackets is the period of the maximum selected in the record of the level measuring station with its percentage deviation from the period of the selected maximum of the section of the GNSS receiver - GNSS satellite record. Periods are reported in mm:ss. A dash indicates missing data or no matched peak identified.